

Level anti-crossings of an NV center in diamond: Decoherence-free subspaces and 3D sensors of microwave magnetic fields

K. Rama Koteswara Rao and Dieter Suter

Fakultät Physik, Technische Universität Dortmund, D-44221 Dortmund, Germany

(Dated: August 22, 2019)

Nitrogen-vacancy (NV) centers in diamond have become an important tool for quantum technologies. All of these applications rely on long coherence times of electron and nuclear spins associated with these centers. Here, we study the energy level anti-crossings of an NV center in diamond coupled to a first-shell ^{13}C nuclear spin in a small static magnetic field. These level anti-crossings occur for specific orientations of the static magnetic field due to the strong non-secular components of the Hamiltonian. At these orientations we observe decoherence-free subspaces, where the electron spin coherence times (T_2^*) are 5-7 times longer than those at other orientations. Another interesting property at these level anti-crossings is that individual transition amplitudes are dominated by a single component of the magnetic dipole moment. Accordingly, this can be used for vector detection of microwave magnetic fields with a single NV center. This is particularly important to precisely control the center using numerical optimal control techniques.

PACS numbers: 03.67.Lx, 76.70.Hb, 33.35.+r, 61.72.J-

I. INTRODUCTION

Nitrogen-Vacancy (NV) centers in diamond have many interesting properties for various applications ranging from quantum information processing to nano-scale imaging [1–5]. For most of these applications, long coherence times of electron and nuclear spins associated with the NV center are essential. Dynamical decoupling pulse sequences are effectively used to decouple NV centers from their environment and hence improve the coherence times of the centers [6–12]. For NV centers, the major source of decoherence is the spin bath formed by the electron and nuclear spins of impurity atoms (e.g. substitutional nitrogen) and ^{13}C nuclear spins in the diamond lattice [13–15]. The coherence times of NV centers can be significantly extended in ultrapure diamond crystals, where the substitutional nitrogen atom concentration is very low. The nuclear spin bath due to ^{13}C can be reduced by using ultrapure diamond crystals enriched with ^{12}C atoms [16]. However, ^{13}C nuclear spins that are strongly coupled to the electron spin of an NV center can also be useful as qubits, either as part of a quantum register [17–20] or for storing quantum information [21]. For example, the ^{13}C nuclear spin of the first coordination-shell has a strong hyperfine coupling with the electron spin of the NV center, which can be used to implement fast multiqubit gates [20, 22]. The disadvantage of using diamond crystals enriched in ^{12}C is that these useful qubits are lost.

In this work, we investigate decoherence-free subspaces at energy level anti-crossings (LACs) of an NV center, whose spin bath is dominated by the ^{13}C nuclear spins. LACs of NV centers that occur between the $m_s = 0$ and $m_s = -1$ spin sublevels of both the ground and optically excited states have been studied extensively and used for various purposes [23–26], such as polarizing the nuclear spins. These anti-crossings occur at magnetic field strengths of ≈ 500 G and ≈ 1000 G. Here, we study

the LACs that occur at much smaller field strengths, of an NV center coupled to a first-shell ^{13}C nuclear spin. Specifically, we study the LACs that occur at two different magnetic field orientations: (i) The strength and orientation of the magnetic field are such that the spectral splitting due to the Zeeman interaction of the electron spin is equal to the splitting due to the hyperfine interaction of the first-shell ^{13}C nuclear spin (≈ 127 MHz). (ii) The magnetic field is oriented in the plane perpendicular to the N-V axis. Close to the LACs, the mixing of the states results in ZERo First-Order Zeeman (ZEFOZ) shift [27–30] of some of the transitions and correspondingly reduced perturbations by magnetic-field noise. This effect manifests itself by long coherence times (T_2^*), almost an order of magnitude longer than at other orientations.

An NV center coupled to a first-shell ^{13}C nuclear spin is particularly attractive for quantum information processing because of the strong hyperfine coupling between the electron and nuclear spins [14, 20–22]. However, harnessing the full potential of this system requires accurate knowledge of the Hamiltonian. The time-independent internal Hamiltonian of this system has been thoroughly investigated [31–33]. In addition, precise knowledge of the time-dependent (microwave) MW Hamiltonian, including the orientation of the MW field with respect to the center, is also important for precise control of the system. This information is particularly important in such centers, since the first-shell ^{13}C nuclear spin breaks the rotational symmetry of the center. At the LACs discussed above, the transition amplitudes of some of the transitions are dominated by a single component of the magnetic dipole moment. This can be used to determine the strength and orientation of the MW magnetic field with a single NV center. A similar vector detection scheme using NV centers was reported in Ref. [34]. However, that required at least three NV centers with different orientations in the focal spot of the objective lens.

This paper is structured as follows. In Sec. II, we discuss the system, its Hamiltonian and the experimental setup. In Secs. III and IV, we analyze the two LACs and discuss the decoherence-free subspaces and the vector detection of MW magnetic fields. Finally, in Sec. V, we draw some conclusions.

II. SYSTEM AND HAMILTONIAN

The system of interest here is a single NV center coupled to a first-shell ^{13}C nuclear spin. Fig. 1(a) shows its structure and defines the coordinate system that we use here. The NV symmetry axis is the z -axis of the center, the x -axis is perpendicular to this axis and lies in the plane containing the vacancy, nitrogen, and the ^{13}C atom, and the y -axis is perpendicular to both of them. The Hamiltonian of the total system consisting of the electron spin ($\mathbf{S} = 1$), the ^{13}C nuclear spin ($\mathbf{I}_1 = 1/2$), and the ^{14}N nuclear spin ($\mathbf{I}_2 = 1$) in this coordinate system can be written as

$$\mathcal{H}_{\text{sys}} = DS_z^2 + \gamma_e \mathbf{B} \cdot \mathbf{S} + \gamma_{n1} \mathbf{B} \cdot \mathbf{I}_1 + \gamma_{n2} \mathbf{B} \cdot \mathbf{I}_2 + PI_{2z}^2 + \mathbf{S} \cdot \mathcal{A}_1 \cdot \mathbf{I}_1 + \mathbf{S} \cdot \mathcal{A}_2 \cdot \mathbf{I}_2. \quad (1)$$

Here, $D = 2.87$ GHz is the electron-spin zero-field splitting, and $\mathbf{B} = B(\sin \theta \cos \phi, \sin \theta \sin \phi, \cos \theta)$ represents the static magnetic field, where θ and ϕ are its polar and azimuthal angles. $P = -4.95$ MHz [35] represents the quadrupolar splitting of the ^{14}N nuclear spin, and \mathcal{A}_1 and \mathcal{A}_2 represent hyperfine tensors of the ^{13}C and ^{14}N nuclear spins respectively with the electron spin. The parameters of the hyperfine tensors are $\mathcal{A}_{1zz} = 128.9$, $\mathcal{A}_{1yy} = 128.4$, $\mathcal{A}_{1xx} = 189.3$, and $\mathcal{A}_{1xz} = 24.1$ MHz [33], and $\mathcal{A}_{2zz} = -2.3$ MHz and $\sqrt{\mathcal{A}_{2xx}^2 + \mathcal{A}_{2yy}^2} = -2.6$ MHz [32, 36, 37].

The Hamiltonian for the coupling of the MW or radio-frequency (RF) field to the electron spin transitions can be written as

$$\mathcal{H}_{\text{mw}} = \sqrt{2}\gamma_e B_{\text{mw}}(\sin \zeta \cos \eta S_x + \sin \zeta \sin \eta S_y + \cos \zeta S_z) \cos(\omega t + \varphi), \quad (2)$$

where B_{mw} , ζ , and η represent the amplitude, polar, and azimuthal angles respectively of the applied field at the site of the NV center. ω and φ represent the frequency and phase of this field.

All the experiments of this work have been performed using a home-built confocal microscope for selective excitation and detection of single NV centers and a MW circuit for resonant excitation of electron spin transitions. A 20 μm thin wire was attached to the diamond surface to generate the MW fields. The used diamond crystal has a natural-abundance ^{13}C concentration and the concentration of substitutional nitrogen centers is < 5 ppb. Studying LACs of the present work requires a precise orientation of the static magnetic field. This was achieved by a permanent magnet attached to two rotational stages

such that their axes are orthogonal to each other and cross at the site of diamond crystal. By rotating the magnet with these rotational stages, a 3D rotation of the magnetic field can be achieved. The strength of the magnetic field (B) at the site of the NV center was 28.9 G.

III. NUCLEAR SPIN INDUCED LAC

First, consider the LACs that occur in the $m_s = \pm 1$ manifold when the energy level splitting due to the Zeeman interaction of the electron spin ($2\gamma_e B \cos \theta$) is equal to the corresponding splitting due to the hyperfine interaction with the ^{13}C nuclear spin, which is ≈ 127 MHz. These LACs have been recently used to study the strong-driving dynamics of a two-level quantum system beyond the rotating-wave approximation [38]. For the magnetic field of strength 28.9 G, these LACs occur when θ is close to 38.4° . The energy level diagram of the system considering only the electron and ^{13}C nuclear spins at this magnetic field orientation is shown in Fig. 1(b). The relevant energy levels for the present work are marked with gray rectangles. Fig. 1(c) shows these levels on an expanded scale as a function of θ of the static magnetic field. As can be seen from this plot, there are many LACs in the $m_s = \pm 1$ manifold when θ is close to 38.4° . Here, we analyze only the LAC at $\theta = 38.4^\circ$, which is marked by the gray oval.

At this magnetic field orientation, the four energy levels (two in the $m_s = 0$ manifold and two in the $m_s = \pm 1$ manifold) marked by small black arrows in Fig. 1(c) are illustrated in Fig. 1(d). We label the corresponding eigenstates as $|\psi_1\rangle$, $|\psi_2\rangle$, $|\psi_3\rangle$, and $|\psi_4\rangle$. In the $|m_s, m_{I_1}, m_{I_2}\rangle$ basis, they are approximately

$$\begin{aligned} |\psi_{1,2}\rangle &\approx \left| 0, \frac{|-\frac{1}{2}\rangle \pm |\frac{1}{2}\rangle}{\sqrt{2}}, 0 \right\rangle, \\ |\psi_{3,4}\rangle &\approx \left| \frac{|-1\rangle \mp |1\rangle}{\sqrt{2}}, -\frac{1}{2}, 0 \right\rangle. \end{aligned} \quad (3)$$

Between these four energy states, five electron spin transitions are possible, which are shown by double sided arrows. Four of these five transitions (thin green and blue arrows) are between the $m_s = 0$ and $m_s = \pm 1$ manifolds and they fall in the MW region, and the fifth transition (thick red arrow), which falls into the RF region, connects the two states of the $m_s = \pm 1$ manifold. The four MW transitions have long coherence times (T_2^*) compared to magnetic field orientations without LACs. This is because, at the LAC, the first-order derivatives of these transition frequencies (ν_i) with respect to the magnetic field are zero, i.e., $\frac{\partial \nu_i}{\partial B} = \frac{\partial \nu_i}{\partial \theta} = \frac{\partial \nu_i}{\partial \phi} = 0$. This is known as ZEFOZ shift [27–30].

Another interesting aspect of these transitions is that they can be excited only by individual Cartesian components of the MW or RF field. For the transitions marked by the letter ‘Y’ (green arrows) in Fig. 1(d),

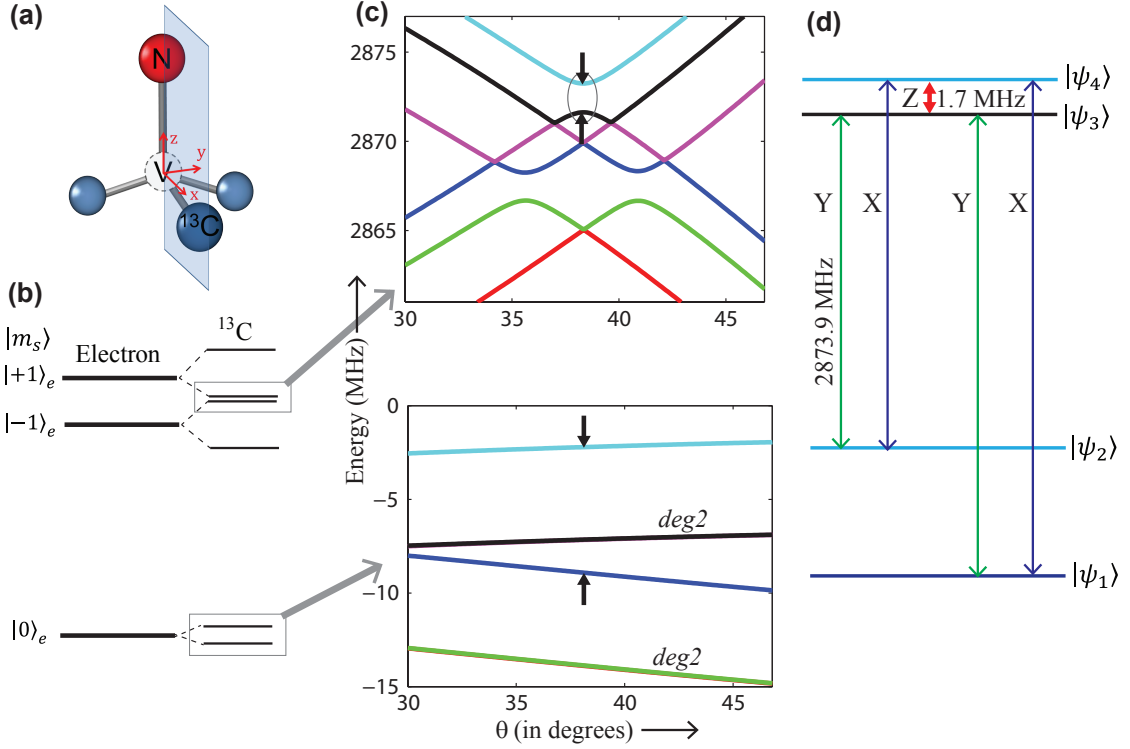


FIG. 1. (a) Structure of an NV center with a ^{13}C atom in the first coordination shell. (b) Energy level diagram of the system considering only the electron and ^{13}C nuclear spins at the LAC point, $2\gamma_e B \cos \theta \approx 127$ MHz. (c) Energy levels in gray rectangles of (b) as a function of θ of a static magnetic field of strength $B = 28.9$ G and $\phi = 0^\circ$. Here, the interaction due to the ^{14}N nuclear spin is also considered. The energy levels labeled by *deg2* are doubly degenerate. (d) Energy levels marked by black arrows in (c) at $\theta = 38.4^\circ$ (LAC) and the possible electron spin transitions between them.

$|\langle\psi_2|S_y|\psi_3\rangle| \approx 0.80$ and $|\langle\psi_1|S_y|\psi_3\rangle| \approx 0.60$ and the corresponding matrix elements of the operators S_x and S_z are approximately zero. This implies that these transitions can be excited only by the y -component of the MW field. Note that from the eigenstates of Eq. 3, the transition amplitudes, $|\langle\psi_2|S_y|\psi_3\rangle| = |\langle\psi_1|S_y|\psi_3\rangle| \approx \frac{1}{\sqrt{2}}$. The actual difference between these quantities is due to the deviations from the approximations in Eq. 3. Similarly, for the transitions marked by the letter ‘X’ (blue arrows) in Fig. 1(d), $|\langle\psi_2|S_x|\psi_4\rangle| \approx 0.80$ and $|\langle\psi_1|S_x|\psi_4\rangle| \approx 0.60$ and the corresponding matrix elements of the operators S_y and S_z are approximately zero. This implies that these transitions can be excited only by the x -component of the MW field. For the transition marked by the letter ‘Z’ (Red arrow) in Fig. 1(d), $|\langle\psi_3|S_z|\psi_4\rangle| \approx 1$ and $|\langle\psi_3|S_x|\psi_4\rangle| = |\langle\psi_3|S_y|\psi_4\rangle| \approx 0$, which implies that this transition can be excited only by the z -component of the RF field. So, in principle, by comparing the experimental transition amplitudes of these transitions, vector detection of applied RF and MW fields can be performed.

In the following, we discuss the experiments performed at this LAC.

Decoherence-free subspaces: To measure the coherence times (T_2^*) of the transitions discussed above, we recorded the optically detected Electron Spin Resonance (ESR)

spectra at the corresponding magnetic field orientation ($\theta = 38.4^\circ$). First, Free Induction Decays (FIDs) were measured by using the Ramsey sequence shown in Fig. 2(a), which were then Fourier transformed to get the frequency domain spectra. The phase of the second MW pulse of the Ramsey sequence was varied with respect to that of the first one as $\varphi = -2\pi\nu_d\tau$, i.e. as a linear function of the delay τ between the pulses. The result is a shift in the measured spectra by an artificial detuning ν_d .

Fig. 2(b) shows the ESR spectra measured between the energy levels of Fig. 1(c). The frequency of the applied MW pulses was 2876.8 MHz. For the upper spectrum, the FID was measured for a duration of $3 \mu\text{s}$ and with a frequency detuning ν_d of 20 MHz. The spectral lines in the frequency range 15-30 MHz correspond to the single-quantum electron spin transitions between the $m_s = 0$ and ± 1 spin sublevels. Along with these, two more transitions appear in the spectrum, one at 6.4 MHz, which is a nuclear spin transition of the $m_s = 0$ subsystem, and the other at 1.7 MHz, which is an electron spin transition within the $m_s = \pm 1$ manifold (marked by thick red arrow in Fig. 1(d)) [38]. These two transitions appear in the spectrum as zero-quantum transitions [33], independent of the detuning ν_d .

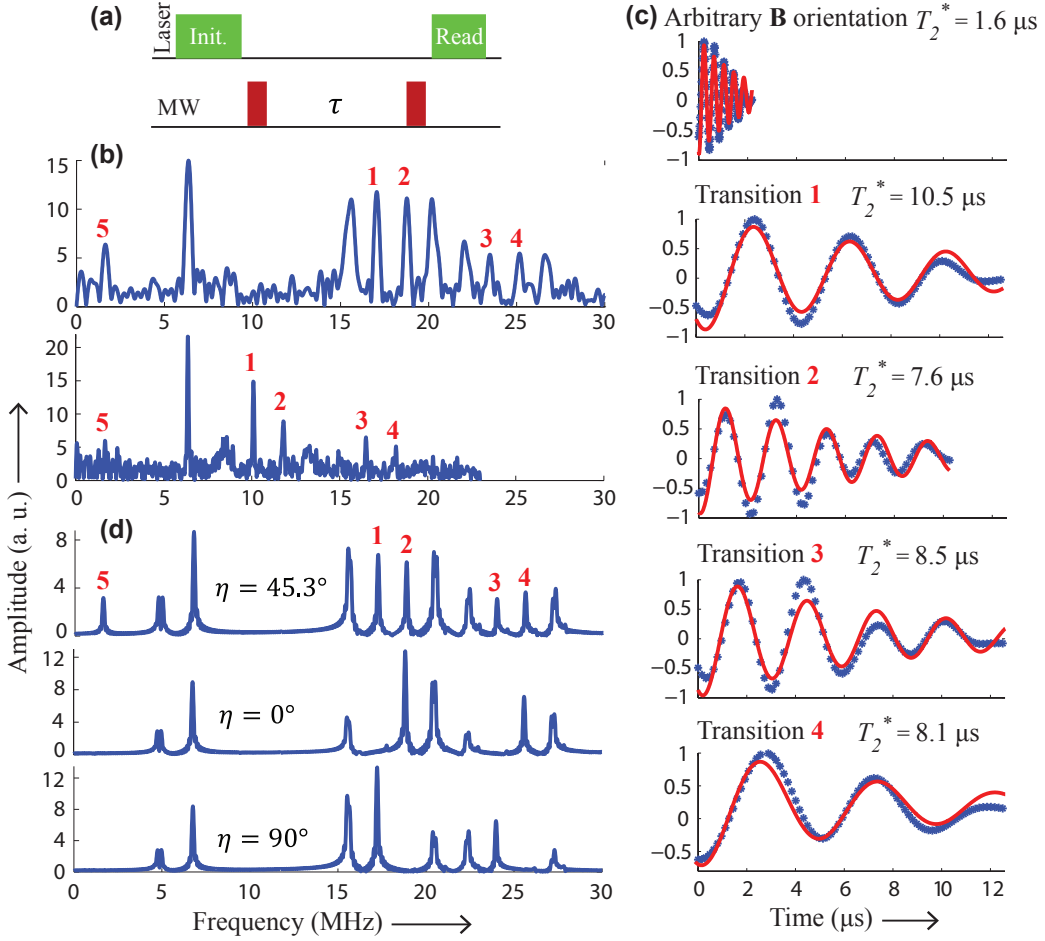


FIG. 2. (a) Pulse sequence to measure FIDs. (b) ESR spectra measured between the energy levels of Fig. 1(c). For the upper and lower spectra, the detuning frequencies (ν_d) were 20 and 13 MHz, and the FID measurement times were 3 and 12 μs respectively. (c) FIDs of the transitions 1-4 along with that of an electron spin transition at an arbitrary \mathbf{B} -field orientation. Blue stars are the data obtained by inverse Fourier transforming the corresponding spectral lines and the red solid lines fit this data to the equation $a \cos(2\pi\nu t) \exp(-t/T_2^*)$. (d) Simulated ESR spectra for different values of η of the MW field. The detuning frequency (ν_d) for the simulation was 20 MHz.

For the lower spectrum of Fig. 2(b), the FID was measured for a duration of 12 μs and with a frequency detuning (ν_d) of 13 MHz. The single quantum transitions correspondingly shift by 7 MHz compared to those in the upper spectrum, whereas the zero-quantum transitions do not. The spectral lines labeled by the numbers 1-5 in both spectra correspond to the five electron spin transitions marked in Fig. 1(d). By comparing the two spectra of Fig. 2(b), it is clear that the transitions labeled by 1-4 have long coherence times (T_2^*) compared to all the other electron spin transitions. As discussed earlier, this is due to the ZEFOZ shift at the LAC.

To quantify the T_2^* of these four transitions, selective FIDs of them were obtained by inverse Fourier transforming the corresponding spectral lines. These are shown in Fig. 2(c) in comparison with that of an electron spin transition at an arbitrary magnetic field orientation, which doesn't have any LAC. The T_2^* of this transition

was measured to be 1.6 (1.3, 1.9) μs and for the transitions 1-4 the values are 10.5 (8.4, 12.6), 7.6 (5.1, 10.0), 8.5 (6.3, 10.6), and 8.1 (6.5, 9.6) μs respectively. This corresponds to an extension of the coherence time by factors of 5-7.

Vector detection of the MW field: For this, we need to determine the strength (B_{mw}) and orientation (angles ζ and η) of the MW field. First, we determine the azimuthal angle (η) of the MW field, which is the angle between the transverse component of the MW field and the x -axis of the NV center. The spectral lines labeled by 1 and 3 in Fig. 2(b) correspond to the transitions between the states $|\psi_2\rangle$ and $|\psi_3\rangle$, and $|\psi_1\rangle$ and $|\psi_3\rangle$ respectively. As discussed earlier, they can be excited only by the y -component of the MW field. Similarly, the spectral lines 2 and 4 correspond to the transitions between the states $|\psi_2\rangle$ and $|\psi_4\rangle$, and $|\psi_1\rangle$ and $|\psi_4\rangle$, respectively and they can be excited only by the x -component of the MW field.

Therefore, from the amplitudes I_α ($\alpha = 1, 2, 3, 4$) of the lines 1...4, the angle, η can be determined as follows.

$$|\tan \eta| = \sqrt{\frac{I_1}{I_2}} = \sqrt{\frac{I_3}{I_4}} \quad (4)$$

For our experimental data, we found $\eta \approx 45.3^\circ$. To test our analysis, we numerically simulated spectra for different values of η . Fig. 2(d) shows the resulting spectra. The top trace, which corresponds to $\eta = 45.3^\circ$ matches the experimental spectrum very well. The middle and bottom traces were simulated for $\eta = 0^\circ$ and 90° respectively. In the middle trace the transitions 1 and 3 are absent whereas in the bottom trace the transitions 2 and 4 are absent. Also, in both of them, the spectral line 5, which corresponds to the electron spin RF transition (1.7 MHz) marked by thick red arrow in Fig. 1(d), is absent. This is expected, because when $\eta = 0^\circ$ or 90° , the MW pulse cannot simultaneously excite the two transitions (1 and 2 or 3 and 4) connecting the two energy levels of this RF transition with the same $m_s = 0$ energy level as one of them has zero transition amplitude.

As discussed earlier, the transitions 1 ($|\psi_2\rangle \leftrightarrow |\psi_3\rangle$) and 5 ($|\psi_3\rangle \leftrightarrow |\psi_4\rangle$) can be excited only by the y - and z -components of the MW and RF fields respectively. This can be used to determine the polar angle (ζ) of the MW field, which is the angle between the MW field and the z -axis of the NV center. For this, we measured the selective Rabi frequencies of the transitions 1 and 5, which are 0.44 (for a MW power of 4.72 mW) and 0.36 MHz (for an RF power of 0.67 mW) respectively. The corresponding expressions can be written as

$$\begin{aligned} \sqrt{2}\gamma_e B_{mw} \sin \zeta \sin \eta |\langle \psi_2 | S_y | \psi_3 \rangle| &= 0.44, \\ \sqrt{2}\gamma_e B_{rf} \cos \zeta |\langle \psi_3 | S_z | \psi_4 \rangle| &= 0.36. \end{aligned}$$

Taking the ratios of these two expressions and substituting the values of η and the transition amplitudes ($|\langle \psi_2 | S_y | \psi_3 \rangle| \approx 0.80$ and $|\langle \psi_3 | S_z | \psi_4 \rangle| \approx 1$), we get, $\tan \zeta = 2.15 \frac{B_{rf}}{B_{mw}}$. The angle ζ was determined by replacing the ratio, $\frac{B_{rf}}{B_{mw}}$ with the corresponding ratio of square roots of measured MW and RF power levels. This value is $\zeta = 39^\circ (-3^\circ, +4^\circ)$. The MW and RF power levels were measured before the diamond sample. After determining the angles, ζ and η , it is possible to determine the amplitudes of the MW and RF fields. From our data, we obtained them as 0.31 and 0.12 G, respectively.

IV. TRANSVERSE FIELD INDUCED LAC

Now, consider the LACs that occur in the $m_s = \pm 1$ manifold when the static magnetic field is oriented in the transverse plane of the NV center, i.e., $\theta = 90^\circ$. The corresponding energy level diagram of the system considering only the electron and ^{13}C nuclear spins is shown

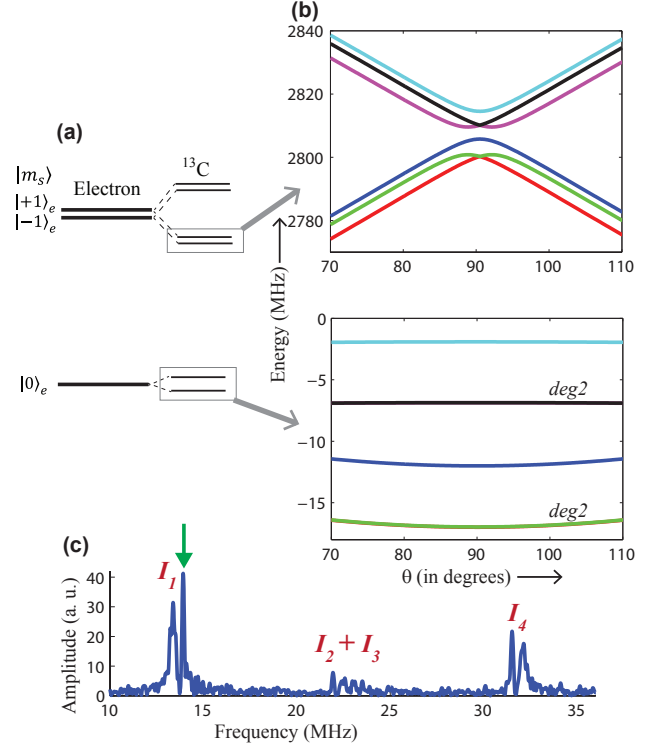


FIG. 3. (a) Energy level diagram of the system considering only the electron and ^{13}C nuclear spins when $\theta = 90^\circ$. (b) Energy levels in the gray rectangles of (a) as a function of θ of the static magnetic field for $\phi = 30^\circ$ and $B = 28.9$ G. Here, the interaction due to the ^{14}N nuclear spin is also considered. The energy levels labeled by *deg2* are doubly degenerate. (c) Experimental ESR spectrum measured between the energy levels of (b) for $\theta = 90^\circ$.

in Fig. 3(a). The energy levels marked by gray rectangles are plotted as a function of the azimuthal angle θ of the static magnetic field in Fig. 3(b), where the interaction with the ^{14}N nuclear spin is also included. From this plot, it is clear that LACs occur in the $m_s = \pm 1$ manifold when $\theta = 90^\circ$. The ESR spectrum measured between these energy levels for $\theta = 90^\circ$ and $\phi = 30^\circ$ is shown in Fig. 3(c).

Decoherence free subspaces: Due to the ZEFOZ shift, the spectral lines have long coherence times (T_2^*) when the B -field is oriented in the xy -plane, compared to other orientations. To compare and quantify the coherence times, we measured the line widths (full width at half height) of the transition marked by green arrow in Fig. 3(c) as a function of θ of the static magnetic field.

The results are shown in Fig. 4. The line widths (of the absolute value spectra) are in the range 0.60 to 0.80 MHz except when θ is in between 85 to 95° , where the line width decreases sharply and reaches a minimum of 0.12 MHz at $\theta = 90^\circ$. This shows that when the static magnetic field is oriented in the transverse plane, the line width decreases by 5-7 times and hence the coherence time (T_2^*) increases by the same order. Similar T_2^*

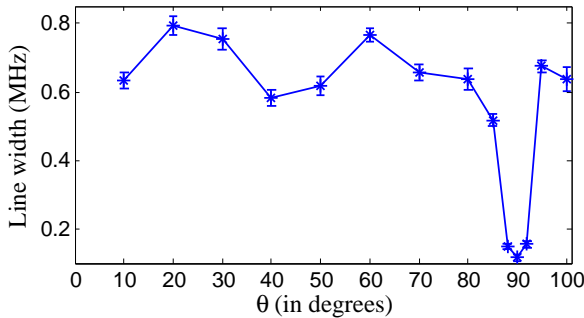


FIG. 4. Line width of the transition marked by green arrow in Fig. 3(c) as a function of θ of the static magnetic field. Stars connected by solid line represent the experimental data and the error bars represent the standard deviation in the measurement of line widths.

improvement has been reported in Ref. [39] for an NV center without any first-shell ^{13}C nuclear spin. The behavior of line width versus θ of Fig. 4 is very similar to the behavior of $1/T_2$ versus θ in Ref. [40]. There, for similar magnetic field strengths, T_2 of ensembles of NV centers was studied as a function of the polar angle θ of the magnetic field in a diamond sample with a high concentration (≈ 100 ppm) of substitutional nitrogen (p1), where the spin bath is dominated by the electron spins. An improvement in T_2 by 2 times was reported when $\theta = 90^\circ$. In contrast to these studies, it has been theoretically predicted [13] and experimentally observed for an ensemble of NV centers [15] that T_2 is maximum when $\theta = 0^\circ$ and minimum when $\theta = 90^\circ$ in diamond crystals with low concentration of substitutional nitrogen, where the spin bath is dominated by the ^{13}C nuclear spins.

Determining the azimuthal angle (η) of the MW field: The amplitudes of the spectral lines shown in Fig. 3(c) are labeled as I_1 , I_2 , I_3 , and I_4 . These amplitudes depend on the azimuthal angle (ϕ) of the static magnetic field and also on the angle (η) between the transverse component of the MW field and the x -axis of the NV center. As discussed in Ref. [33], this dependence can be used to determine the angle η . For this purpose, we measured the amplitudes I_1 to I_4 as a function of ϕ of the static magnetic field when $\theta = 90^\circ$.

The experimental data along with the numerically simulated ones are shown in Fig. 5. Blue stars and red triangles represent the experimentally measured quantities $(I_1 + I_4)/(I_2 + I_3)$ and $(I_2 + I_3)/(I_1 + I_4)$ respectively. Blue solid and red dashed lines represent the corresponding simulated quantities. For the simulation, $\eta = 45.3^\circ$, which was determined in Sec. III, has been used. The simulated quantities are in good agreement with the experimental ones, which confirms that the angle η determined in Sec. III is correct.

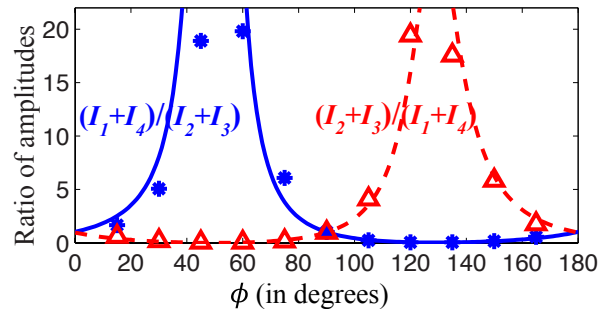


FIG. 5. Ratios of amplitudes of spectral lines as a function of ϕ of the static magnetic field for $\theta = 90^\circ$.

V. CONCLUSION

We have studied, experimentally and theoretically, two energy level anti-crossings in an NV center coupled to a first-shell ^{13}C nuclear spin in a small static magnetic field. These anti-crossings occur in the $m_s = \pm 1$ manifolds due to the strong non-secular components of the Hamiltonian for two different static magnetic field orientations: (i) When the energy level splitting due to the Zeeman interaction of the electron spin is equal to the splitting due to the hyperfine interaction of the ^{13}C nuclear spin (≈ 127 MHz). (ii) When the magnetic field is oriented in the transverse plane of the NV center. At both of these LACs, we observed decoherence free subspaces due to the ZEFOZ shift, i.e., the coherence times (T_2^*) of some of the transitions are up to 7 times longer than those at other orientations of the magnetic field. At these LACs, some of the electron spin transition amplitudes are dominated by a single component of the magnetic dipole moment. This has been used to perform vector detection of the MW magnetic field by a single NV center. The azimuthal angle of the MW field with respect to the atomic structure of the center has been determined accurately, but the accuracy of the determined polar angle of the MW field is limited. This is due to the impedance mismatches in the MW circuit caused by the copper wire attached to the diamond surface by which the MW fields are generated. However, with a near perfect impedance matching MW circuit, the polar angle can be determined more accurately. The presented scheme will be useful for vector microwave magnetometry by a single spin. Determining the orientation of the MW field is also important to precisely control the NV center using optimal control techniques as the center is not symmetric with respect to the NV axis due to the presence of ^{13}C atom in the first-shell.

ACKNOWLEDGMENTS

We thank Jingfu Zhang for useful discussions. This work was supported by the DFG through grant no. Su

-
- [1] M. W. Doherty, N. B. Manson, P. Delaney, F. Jelezko, J. Wrachtrup, and L. C. Hollenberg, *Physics Reports* **528**, 1 (2013).
- [2] L. Childress and R. Hanson, *MRS Bulletin* **38**, 134 (2013).
- [3] S. Hong, M. S. Grinolds, L. M. Pham, D. L. Sage, L. Luan, R. L. Walsworth, and A. Yacoby, *MRS Bulletin* **38**, 155 (2013).
- [4] R. Schirhagl, K. Chang, M. Loretz, and C. L. Degen, *Annual Review of Physical Chemistry* **65**, 83 (2014).
- [5] L. Rondin, J.-P. Tetienne, T. Hingant, J.-F. Roch, P. Maletinsky, and V. Jacques, *Reports on Progress in Physics* **77**, 056503 (2014).
- [6] C. A. Ryan, J. S. Hodges, and D. G. Cory, *Phys. Rev. Lett.* **105**, 200402 (2010).
- [7] G. de Lange, Z. H. Wang, D. Ristè, V. V. Dobrovitski, and R. Hanson, *Science* **330**, 60 (2010).
- [8] T. van der Sar, Z. H. Wang, M. S. Blok, H. Bernien, T. H. Taminiau, D. M. Toyli, D. A. Lidar, D. D. Awschalom, R. Hanson, and V. V. Dobrovitski, *Nature* **484**, 82 (2012).
- [9] J. H. Shim, I. Niemeyer, J. Zhang, and D. Suter, *EPL (Europhysics Letters)* **99**, 40004 (2012).
- [10] J. Zhang, A. M. Souza, F. D. Brandao, and D. Suter, *Phys. Rev. Lett.* **112**, 050502 (2014).
- [11] J. Zhang and D. Suter, *Phys. Rev. Lett.* **115**, 110502 (2015).
- [12] N. Bar-Gill, L. Pham, A. Jarmola, D. Budker, and R. Walsworth, *Nature Communications* **4**, 1743 (2013).
- [13] J. R. Maze, J. M. Taylor, and M. D. Lukin, *Phys. Rev. B* **78**, 094303 (2008).
- [14] N. Mizuochi, P. Neumann, F. Rempp, J. Beck, V. Jacques, P. Siyushev, K. Nakamura, D. J. Twitchen, H. Watanabe, S. Yamasaki, F. Jelezko, and J. Wrachtrup, *Phys. Rev. B* **80**, 041201 (2009).
- [15] P. L. Stanwix, L. M. Pham, J. R. Maze, D. Le Sage, T. K. Yeung, P. Cappellaro, P. R. Hemmer, A. Yacoby, M. D. Lukin, and R. L. Walsworth, *Phys. Rev. B* **82**, 120101 (2010).
- [16] G. Balasubramanian, P. Neumann, D. Twitchen, M. Markham, R. Kolesov, N. Mizuochi, J. Isoya, J. Achard, J. Beck, J. Tissler, V. Jacques, P. R. Hemmer, F. Jelezko, and J. Wrachtrup, *Nature Materials* **8**, 383 (2009).
- [17] L. Childress, M. V. Gurudev Dutt, J. M. Taylor, A. S. Zibrov, F. Jelezko, J. Wrachtrup, P. R. Hemmer, and M. D. Lukin, *Science* **314**, 281 (2006).
- [18] M. V. G. Dutt, L. Childress, L. Jiang, E. Togan, J. Maze, F. Jelezko, A. S. Zibrov, P. R. Hemmer, and M. D. Lukin, *Science* **316**, 1312 (2007).
- [19] T. H. Taminiau, J. Cramer, T. van der Sar, V. V. Dobrovitski, and R. Hanson, *Nature nanotechnology* **9**, 171 (2014).
- [20] P. Neumann, N. Mizuochi, F. Rempp, P. Hemmer, H. Watanabe, S. Yamasaki, V. Jacques, T. Gaebel, F. Jelezko, and J. Wrachtrup, *Science* **320**, 1326 (2008).
- [21] J. H. Shim, I. Niemeyer, J. Zhang, and D. Suter, *Phys. Rev. A* **87**, 012301 (2013).
- [22] F. Jelezko, T. Gaebel, I. Popa, M. Domhan, A. Gruber, and J. Wrachtrup, *Phys. Rev. Lett.* **93**, 130501 (2004).
- [23] X.-F. He, N. B. Manson, and P. T. H. Fisk, *Phys. Rev. B* **47**, 8809 (1993).
- [24] R. J. Epstein, F. M. Mendoza, Y. K. Kato, and D. D. Awschalom, *Nature Physics* **1**, 94 (2005).
- [25] V. Jacques, P. Neumann, J. Beck, M. Markham, D. Twitchen, J. Meijer, F. Kaiser, G. Balasubramanian, F. Jelezko, and J. Wrachtrup, *Phys. Rev. Lett.* **102**, 057403 (2009).
- [26] B. Smeltzer, J. McIntyre, and L. Childress, *Phys. Rev. A* **80**, 050302 (2009).
- [27] E. Fraval, M. J. Sellars, and J. J. Longdell, *Phys. Rev. Lett.* **92**, 077601 (2004).
- [28] E. Fraval, M. J. Sellars, and J. J. Longdell, *Phys. Rev. Lett.* **95**, 030506 (2005).
- [29] J. J. Longdell, A. L. Alexander, and M. J. Sellars, *Phys. Rev. B* **74**, 195101 (2006).
- [30] M. Lovrić, P. Glasenapp, D. Suter, B. Tumino, A. Ferrier, P. Goldner, M. Sabooni, L. Rippe, and S. Kröll, *Phys. Rev. B* **84**, 104417 (2011).
- [31] J. H. N. Loubser and J. A. van Wyk, *Reports on Progress in Physics* **41**, 1201 (1978).
- [32] S. Felton, A. M. Edmonds, M. E. Newton, P. M. Martineau, D. Fisher, D. J. Twitchen, and J. M. Baker, *Phys. Rev. B* **79**, 075203 (2009).
- [33] K. R. K. Rao and D. Suter, *Phys. Rev. B* **94**, 060101 (2016).
- [34] P. Wang, Z. Yuan, P. Huang, X. Rong, M. Wang, X. Xu, C. Duan, C. Ju, F. Shi, and J. Du, *Nature Communications* **6**, 6631 (2015).
- [35] C. S. Shin, M. C. Butler, H.-J. Wang, C. E. Avalos, S. J. Seltzer, R.-B. Liu, A. Pines, and V. S. Bajaj, *Phys. Rev. B* **89**, 205202 (2014).
- [36] X.-F. He, N. B. Manson, and P. T. H. Fisk, *Phys. Rev. B* **47**, 8816 (1993).
- [37] M. Chen, M. Hirose, and P. Cappellaro, *Phys. Rev. B* **92**, 020101 (2015).
- [38] K. R. K. Rao and D. Suter, *arXiv:1610.04512 [quant-ph]* (2016).
- [39] F. Dolde, H. Fedder, M. W. Doherty, T. Nobauer, F. Rempp, G. Balasubramanian, T. Wolf, F. Reinhard, L. C. L. Hollenberg, F. Jelezko, and J. Wrachtrup, *Nature Physics* **7**, 459 (2011).
- [40] C. S. Shin, C. E. Avalos, M. C. Butler, H.-J. Wang, S. J. Seltzer, R.-B. Liu, A. Pines, and V. S. Bajaj, *Phys. Rev. B* **88**, 161412 (2013).